

Cooperative epithelial phagocytosis enables error correction in the early embryo

<https://doi.org/10.1038/s41586-021-03200-3>

Received: 12 December 2019

Accepted: 24 December 2020

Published online: 10 February 2021

 Check for updates

Esteban Hoijman¹, Hanna-Maria Häkkinen¹, Queralt Tolosa-Ramon¹, Senda Jiménez-Delgado¹, Chris Wyatt¹, Marta Miret-Cuesta¹, Manuel Irimia^{1,2,3}, Andrew Callan-Jones⁴, Stefan Wieser⁵ & Verena Ruprecht^{1,2}

Errors in early embryogenesis are a cause of sporadic cell death and developmental failure^{1,2}. Phagocytic activity has a central role in scavenging apoptotic cells in differentiated tissues^{3–6}. However, how apoptotic cells are cleared in the blastula embryo in the absence of specialized immune cells remains unknown. Here we show that the surface epithelium of zebrafish and mouse embryos, which is the first tissue formed during vertebrate development, performs efficient phagocytic clearance of apoptotic cells through phosphatidylserine-mediated target recognition. Quantitative four-dimensional *in vivo* imaging analyses reveal a collective epithelial clearance mechanism that is based on mechanical cooperation by two types of Rac1-dependent basal epithelial protrusions. The first type of protrusion, phagocytic cups, mediates apoptotic target uptake. The second, a previously undescribed type of fast and extended actin-based protrusion that we call ‘epithelial arms’, promotes the rapid dispersal of apoptotic targets through Arp2/3-dependent mechanical pushing. On the basis of experimental data and modelling, we show that mechanical load-sharing enables the long-range cooperative uptake of apoptotic cells by multiple epithelial cells. This optimizes the efficiency of tissue clearance by extending the limited spatial exploration range and local uptake capacity of non-motile epithelial cells. Our findings show that epithelial tissue clearance facilitates error correction that is relevant to the developmental robustness and survival of the embryo, revealing the presence of an innate immune function in the earliest stages of embryonic development.

Early embryogenesis is prone to cellular errors such as mitotic defects that are induced by cell intrinsic or extrinsic stress factors^{1,2}. This leads to sporadic cell death of progenitor stem cells^{7–10}, which is assumed to be a major cause of early developmental failures in human pre-implantation development^{11,12}. Detection and removal of cell corpses requires a clearance mechanism similar to that mediated by professional phagocytic cells in adult tissues¹³. Whether such active mechanisms for efficient clearance of apoptotic cells exist in the early blastula and gastrula stages of vertebrate development is still not understood.

Epithelial clearance in the early embryo

At the early blastula stage, the vertebrate embryo consists of an undifferentiated inner cell mass covered by a squamous surface epithelium, termed the epithelial enveloping layer (EVL) in zebrafish and the trophoblast in mouse. To identify how apoptotic events are managed during early embryogenesis, we performed quantitative four-dimensional *in vivo* imaging of single apoptotic cell dynamics in the zebrafish blastula. Spontaneous progenitor cell death occurred and showed typical

hallmarks of apoptosis such as changes in the cell shape (Fig. 1a, Supplementary Video 1), cell and nuclear fragmentation (Fig. 1a, Extended Data Fig. 1a, b and Supplementary Video 1), phosphatidylserine (PS) exposure (Extended Data Fig. 1a and Supplementary Video 1) and Caspase-3 activation (Extended Data Fig. 1c and Supplementary Video 1). Apoptotic events were frequently associated with errors in cell division such as aberrations in chromosome segregation (Extended Data Fig. 1b and Supplementary Videos 2, 11). Notably, three-dimensional tracking of apoptotic progenitor cells revealed their accumulation inside the EVL (Fig. 1a, Extended Data Fig. 1b, c and Supplementary Video 1), which suggests that epithelial cells in the early embryo have a specific uptake ability.

We next challenged zebrafish blastula embryos by ectopically inducing apoptosis through mosaic overexpression of the pro-apoptotic protein Bax¹⁴ (Bax⁺ cells), visualized by PS exposure (Extended Data Figs. 1d, 10) and Caspase-3 activation (Extended Data Fig. 1e, e' and Supplementary Video 3). Embryos survived in conditions of abundant cell death (Fig. 1b, c), which suggests that an efficient failure-compensation program exists. Extensive uptake of Bax⁺ cells by the epithelium revealed

¹Centre for Genomic Regulation (CRG), The Barcelona Institute of Science and Technology, Barcelona, Spain. ²Universitat Pompeu Fabra (UPF), Barcelona, Spain. ³ICREA, Barcelona, Spain.

⁴Laboratoire Matière et Systèmes Complexes, CNRS/Université de Paris, UMR 7057, Paris, France. ⁵Institut de Ciències Fotòniques (ICFO), The Barcelona Institute of Science and Technology, Castelldefels, Spain. ✉e-mail: hoijman@gmail.com; stefan.wieser@icfo.eu; verena.ruprecht@crgeu

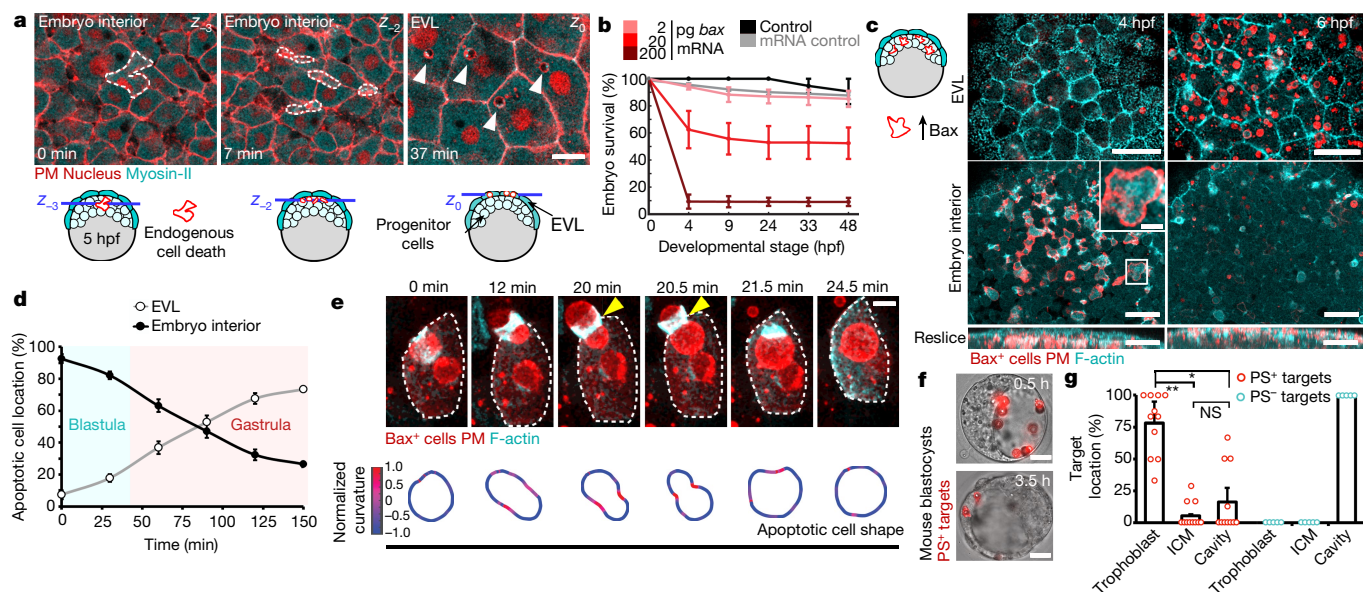


Fig. 1 | The embryonic surface epithelium performs efficient phagocytic clearance of apoptotic cells. **a**, Endogenous cell death of a single progenitor cell (dashed lines) showing cell shape loss (0 min), fragmentation (7 min) and epithelial uptake (37 min) in a *Tg(actb1:Myf12.1-eGFP)* embryo co-expressing *Lyn*-tdTomato (plasma membrane (PM)) and H2A-mCherry (nucleus). The imaging plane (z) is depicted in the sketch. Arrowheads indicate particles localized inside the EVL. **b**, Embryo survival curves of unperturbed wild-type embryos (control, $n = 261$), mosaic embryos expressing *Lyn*-tdTomato alone (mRNA control, $n = 238$) or in combination with the indicated *bax* mRNA levels (2 pg, $n = 236$ embryos; 20 pg, $n = 176$ embryos; 200 pg, $n = 319$ embryos). **c**, Representative images of *Tg(actb1:Lifeact-GFP)* embryos with mosaic co-expression of Bax (2 pg *bax* mRNA) and *Lyn*-tdTomato (plasma membrane) leading to 48.6 ± 6.3 apoptotic cells in a field of view of $2.1 \pm 0.2 \times 10^6 \mu\text{m}^3$ ($n = 5$ embryos), showing EVL uptake versus clearance of the embryo interior over time (hours post fertilization (hpf)). **d**, Quantitative clearance dynamics of Bax⁺

cells ($n = 6$ embryos). **e**, Top, maximum z-projections of a single epithelial cell (dashed line) expressing epithelium-specific Lifeact-GFP, showing the phagocytic uptake of an apoptotic Bax⁺ cell in vivo. Arrowheads indicate high apoptotic cell deformations, represented by colour-coded normalized curvatures (bottom). Epithelial F-actin is shown in cyan. **f**, Clearance of PS⁺ surrogate apoptotic targets (glass spheres coated with PS, POPC (1-palmitoyl-2-oleoyl-*sn*-glycero-3-phospholcoline) and TexasRed-DHPE (1,2-dihexadecanoyl-*sn*-glycero-3-phosphoethanolamine) injected into the mouse blastocyst cavity. The time after injection (h) is indicated for each image. **g**, Quantification of PS⁺ and PS⁻ target localization at 3.5 h after injection. ICM, inner cell mass. $n = 11$ and 5 embryos for PS⁺ and PS⁻ targets, respectively. Paired Friedman test and Dunn's multiple comparison test with adjusted *P* values. ***P* = 0.0042; **P* = 0.0315; NS, not significant (*P* > 0.999). Scale bars, 20 μm (a, e, f), 50 μm (c) and 10 μm (c; inset). Data are mean \pm s.e.m. (b, d, g).

a high clearance capacity of this embryonic epithelium (Fig. 1c, d and Supplementary Video 3), with average removal rates of 68 ± 3 apoptotic particles within 2 h in the field of view. Similar clearance was observed for mosaic activation of the apoptotic effector molecule Caspase-8^{ERT2} (Extended Data Fig. 1f and Supplementary Video 4). By contrast, progenitor cells showed a very low uptake rate (Extended Data Fig. 1g), supporting the idea that apoptotic cell clearance is epithelium-specific.

Epithelial clearance occurred under variable intrinsic and extrinsic stress factors that trigger cell death: (1) impairing of DNA replication by mosaic overexpression of a mutant form of topoisomerase-II¹⁵; (2) transplantation of ultraviolet-light (UV)-irradiated cells; and (3) pharmacologically induced mitochondrial stress using Raptinal¹⁶ (Extended Data Figs. 1h–m, 10 and Supplementary Video 4). These data indicate that epithelial clearance does not depend on a specific apoptotic inducer and that the whole epithelium is competent for uptake. Transplantation of only a few apoptotic cells (4 ± 3 cells, Extended Data Fig. 1n) or single-cell induction of programmed progenitor cell death by two-photon illumination (Extended Data Fig. 1o and Supplementary Video 4) was sufficient to elicit epithelial uptake, further indicating its high sensitivity. Together, these observations establish epithelial clearance as an error-correction mechanism that is present at the blastula stages of embryonic development.

Mechanisms of epithelial phagocytosis

Single-cell imaging of epithelial uptake dynamics in vivo showed the formation of characteristic phagocytic cups, which are dynamic actin-rich structures at the basal epithelial surface that faces the embryo interior

(Fig. 1e, Extended Data Fig. 2a and Supplementary Video 5). During engulfment, an F-actin ring formed at the pseudopod front around the apoptotic target (Fig. 1e, Extended Data Fig. 2a, b and Supplementary Video 5), associated with target deformations that are indicative of localized mechanical compression forces exerted by phagocytic cups (Fig. 1e, Extended Data Fig. 2a–d and Supplementary Video 5). Actin further enriched at the cup closure site accompanied by local inward bending of the target (Fig. 1e and Supplementary Video 5), suggesting that the target is being pushed into the epithelial cell¹⁷. Phagocytic cups formed at the basal surface from both medial and lateral regions, with the latter also extending continuously active membrane ruffles¹⁸ (Extended Data Fig. 2e, f and Supplementary Video 5). Apoptotic cell splitting was observed during phagocytic cup formation, leading to iterative apoptotic cell fragmentation underlying the wide range of phagocytosed particle sizes that were observed in epithelial cells (Extended Data Fig. 2g).

The GTPase Rac1 mediates apoptotic phagocytosis in multiple physiological and pathological contexts^{3,6}. Genetic interference using a dominant-negative form of Rac1 (dnRac1) expressed in single epithelial cells blocked phagocytic uptake (Extended Data Fig. 2h, i). Pharmacological interference with PI3K, a kinase that regulates phagocytic cup dynamics¹⁹, showed that its activity is also required for uptake (Extended Data Fig. 2j, k), establishing that epithelial phagocytosis is mediated by a Rac1-PI3K-dependent signalling pathway.

Analysis of vesicles formed upon apoptotic target ingestion showed that these vesicles represent functional phagosomes: plasma membranes from both the phagocyte and target were present (Extended Data Fig. 2l, m), the vesicles generated superoxide anions (Extended Data Fig. 2n) and the internal vesicle content was degraded over time

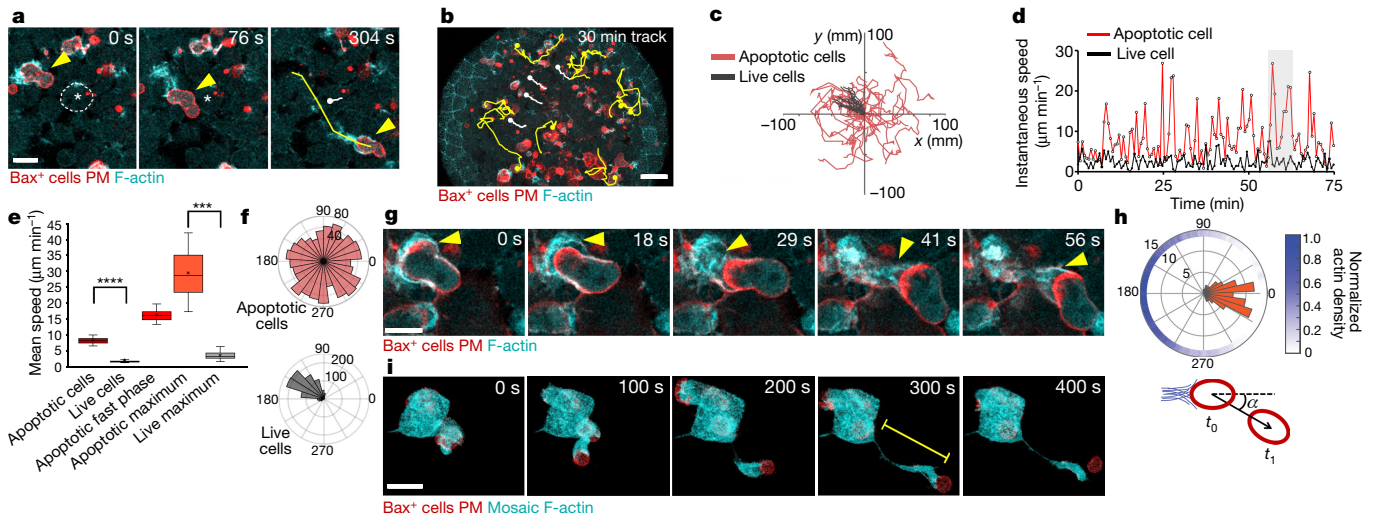


Fig. 2 | Apoptotic cells acquire fast motility associated with actin-based epithelial arm protrusions. **a**, Motility of a single apoptotic Bax⁺ cell (arrowhead) compared with a live progenitor cell (dashed line, asterisk) and their total path lengths (yellow and white lines, respectively) in a *Tg(actb1:Lifeact-GFP)* embryo. **b**, Three-dimensional in vivo tracking of apoptotic and live cell motility (yellow and white lines, respectively; 30 min period). **c**, Representative *xy* trajectories of apoptotic and live cells centred to the origin; live cells show directionality as part of their gastrulation movements. **d**, Instantaneous cell speed fluctuations of an apoptotic cell and a live cell. The grey region represents a phase of fast motility. **e**, Mean instantaneous cell speeds ($n = 28$ and 25 apoptotic and live cells, respectively, from 4 embryos). Box plot shows the maximum and minimum (whiskers),

medians (lines), 25th and 75th percentiles (boxes) and means (crosses). Unpaired two-sided *t*-test. **** $P < 1 \times 10^{-15}$; *** $P = 8 \times 10^{-15}$. **f**, Angle distribution of tracks of apoptotic and live cells ($n = 29$ and 23 cells, respectively, from 4 embryos). **g**, In vivo dynamics of a single apoptotic Bax⁺ cell associated with an external F-actin accumulation (arrowheads) in a *Tg(actb1:Lifeact-GFP)* embryo. **h**, Angle histogram of cell movement directions (α , red) between t_0 and t_1 ($t_{lag} = 60$ s) and external F-actin localization (blue) at t_0 along a circle, which reflects the normalized apoptotic cell perimeter (87 direction changes and density profiles, $n = 15$ cells from 3 embryos). **i**, Epithelial arm protrusion visualized using mosaic Lifeact-GFP expression (total length, $45 \mu\text{m}$; yellow line). Scale bars, $20 \mu\text{m}$ (**a**, **g**), $50 \mu\text{m}$ (**b**) and $10 \mu\text{m}$ (**i**).

(Extended Data Fig. 20–r and Supplementary Video 5). In agreement with a known role of integrins in phagocytosis²⁰, we further identified Itga5 as a marker of epithelial phagosomes (Extended Data Fig. 2s).

PS exposure by apoptotic cells mediates apoptotic cell recognition and uptake by professional phagocytes²¹. Injection of the PS-binding protein annexin-V significantly impaired apoptotic cell clearance (Extended Data Fig. 3a, b). Transplantation of lipid-based surrogate apoptotic targets confirmed that the presence of PS (PS⁺) was required and sufficient for the in vivo recognition and epithelial phagocytosis of these surrogate particles (Extended Data Fig. 3c–e and Supplementary Video 6). Injection of a high number of PS-negative (PS⁻) surrogate targets caused abundant developmental failure, whereas PS addition to the surrogate targets improved the survival of the embryo (Extended Data Fig. 3f). Cross-species transplantation of UV-irradiated apoptotic human Jurkat T cells into zebrafish embryos further confirmed phagocytic uptake by conserved target surface properties (Extended Data Fig. 3g, h). These data suggest that PS-dependent mechanisms mediate tissue clearance and restoration of embryo homeostasis.

To analyse the global gene expression profile involved in phagocytic epithelial functions, we performed RNA sequencing on EVL and progenitor cells of the blastula embryo. Upregulated EVL genes were enriched in functions associated with phagocytosis, such as ‘endocytosis’ and ‘early, late and recycling endosomes’ (Extended Data Fig. 3i and Supplementary Table 1). Key genes of the phagocytic machinery were also upregulated in the EVL tissue compared with progenitor cells, such as *rab7a*²², *waslb*²³, *dnm2a*²⁴ (*Rab7*, *Wasl* and *Dnm2* in mammals) and other relevant genes for phagocytosis (including *raba1c*, *pld1b*, *asap2b*, *chmp4bb*, *cyth1a*, *wipf2a* and *iqsec1b*). Multiple terms related to innate immune functions and repair response were also enriched among upregulated genes in the EVL (Extended Data Fig. 3i and Supplementary Table 1), suggesting a possible immuno-protective role of the surface epithelium in the early embryo beyond a phagocytic clearance function.

Altogether, these results indicate that the EVL performs active clearance in the early embryo by phagocytic uptake of apoptotic cells, using similar mechanisms to those described for professional phagocytes¹³.

Conservation of embryonic clearance

Embryonic cell aggregates that self-organize and form a surface epithelium were observed to show phagocytic epithelial activity (Extended Data Figs. 4a, 10), indicating a primordial physiological tissue clearance function. To evaluate the evolutionary conservation of epithelial scavenging in early mammalian development, we investigated apoptotic cell dynamics in mouse blastocysts. Time-lapse imaging revealed endogenous apoptotic events, with cells being extruded into the blastocyst cavity and later ingested by the trophoblast (Extended Data Fig. 4b, b', c and Supplementary Video 7). Similarly, transplanted apoptotic mouse embryonic stem cells were mostly ingested by trophoblast cells (Extended Data Figs. 4d–g, 10 and Supplementary Video 7). Transferring surrogate apoptotic targets into the blastocyst cavity confirmed that uptake by trophoblast cells is PS-dependent (Fig. 1f, g and Extended Data Fig. 4h). A gene ontology enrichment analysis of upregulated trophoblast genes compared with the inner cell mass from public RNA-sequencing data²⁵ of pre-implantation mouse blastocysts revealed terms in common with the zebrafish EVL, such as ‘endocytosis’ and ‘immune-related’ functions (Extended Data Fig. 3j and Supplementary Table 1). Similar enriched functions were documented for human trophoblast²⁶ (Supplementary Table 1). These results suggest that the apoptotic phagocytic capacity of the surface embryonic epithelium is conserved in mammals.

Epithelial cells move apoptotic targets

Epithelia form stably connected tissues with a restricted cellular range for phagocytic target search and capture that is different from

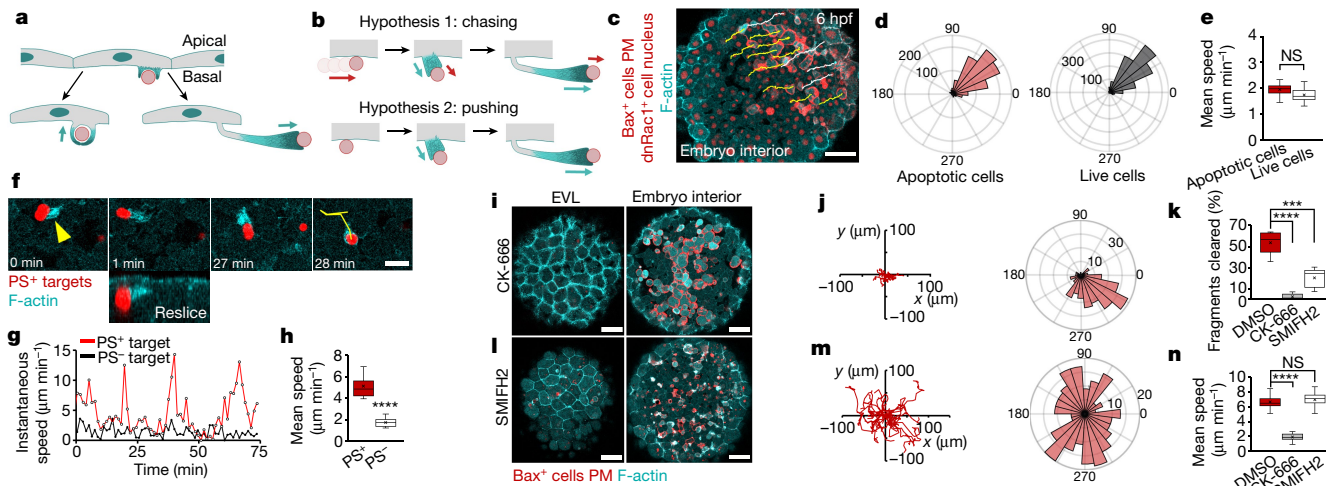


Fig. 3 | Epithelial arms mechanically push apoptotic cells. **a**, Epithelial cells show two types of actin-based basal protrusions: phagocytic cups (left) and epithelial arms (right). **b**, Two possible interaction mechanisms between epithelial arms and apoptotic cells (see ‘Epithelial cells move apoptotic targets’ for details). **c**, Representative *xy* trajectories from three-dimensional tracking of mosaic apoptotic Bax⁺ and live cells (yellow and white, respectively) in embryos ubiquitously co-expressing dnRac1 and H2A–mCherry (dnRac1⁺ cells). **d**, Angle distributions of cells from **c** ($n = 18$ and 22 apoptotic and live cells, respectively, from 3 embryos). **e**, Mean instantaneous cell speeds of apoptotic and live cells ($n = 22$ and 20 cells, respectively, from 4 embryos) in embryos expressing dnRac1. **f**, Motility of PS⁺ surrogate apoptotic targets in association with F-actin from epithelial arms (arrowhead) and total path length (yellow line) over the indicated period. **g**, Instantaneous speed fluctuations of lipid aggregates containing or lacking PS (PS⁺ and PS⁻ targets, respectively). **h**, Mean

instantaneous speed of PS⁺ and PS⁻ surrogate targets ($n = 26$ and 23 from 6 and 5 embryos, respectively). **i–n**, Clearance of apoptotic cells in the presence of CK-666 or SMIFH2. Representative images (**i**), *xy* trajectories (**j**, **m**, left) and angle distributions (**j**, **m**, right) for apoptotic cells ($n = 18$ and 26 from 3 CK666- and 4 SMIFH2-treated embryos, respectively). **k**, **n**, Quantification of phagocytic epithelial clearance (**k**; $n = 9$ DMSO-, 6 CK-666-, 4 SMIFH2-treated embryos) and mean instantaneous speed (**n**; $n = 38$, 27 cells from 8 DMSO-, 3CK-666-, 3SMIFH2-treated *Tg(actb1:Lifeact-GFP)* embryos). **e**, **h**, Unpaired two-sided *t*-test (NS, $P = 0.107396$ (**e**); $****P < 1 \times 10^{-15}$ (**h**)). **k**, **n**, Unpaired one-way ANOVA and Tukey’s multiple comparison test ($****P = 5.38 \times 10^{-9}$, $***P = 3.21 \times 10^{-6}$ (**k**); $****P = 3.99 \times 10^{-10}$, NS, $P = 0.320128$ (**n**)). Box plots show the maximum and minimum (whiskers), medians (lines), 25th and 75th percentiles (boxes) and means (crosses). Scale bars, $50 \mu\text{m}$ (**c**, **i**, **l**) and $20 \mu\text{m}$ (**f**).

professional phagocytes, which have migratory abilities¹³. Unexpectedly, *in vivo* tracking of single apoptotic Bax⁺ cells revealed fast and non-directional movement with mean velocity (v) = $8.3 \pm 0.2 \mu\text{m min}^{-1}$ (mean \pm s.e.m.) and peak velocities of up to $30.1 \pm 1.5 \mu\text{m min}^{-1}$ (Fig. 2a–f and Supplementary Video 8), in comparison to the slow and directional movements of neighbouring live cells ($\langle v \rangle = 1.8 \pm 0.1 \mu\text{m min}^{-1}$) (Fig. 2a–f and Supplementary Video 8).

We found that phases of fast apoptotic movement were correlated with an accumulation of external F-actin in contact with the apoptotic cell rear opposite to its movement direction (Fig. 2g, h, Extended Data Fig. 5a, b and Supplementary Videos 8, 9). Epithelium-specific staining revealed that the actin accumulations originate from epithelial cells upon interaction with apoptotic cells (Extended Data Fig. 5c), forming thin elongated basal protrusions that were coordinated with apoptotic movement (Fig. 2i, Extended Data Fig. 5d and Supplementary Video 10). Protrusion fronts showed strong actin enrichment and retrograde actin flow (Extended Data Fig. 5e, f). Given the dynamic extension and retraction of these epithelial protrusions and their close physical association with motile apoptotic targets, we termed the protrusions ‘epithelial arms’, reminiscent of an arm handling an object. Epithelial arm protrusions occurred at comparable rates to phagocytic cups (61.6 ± 9.7 arms per hour and 40.8 ± 3.5 phagocytic cups per hour; 165.3 ± 6.1 EVL cells in the field of view, $n = 3$ embryos). Apoptotic motility and epithelial arm formation was also observed for endogenously dying cells (Extended Data Fig. 6a, b and Supplementary Videos 1, 11) and ectopically induced cell death via Caspase-8^{ERT2} (Extended Data Fig. 6c–e) and mutant topoisomerase-II (Extended Data Fig. 6f–h), or after transplantation of apoptotic Jurkat T cells (Extended Data Fig. 6i and Supplementary Video 12) and UV-irradiated cells (Extended Data Fig. 6j and Supplementary Video 12).

The coordination between epithelial arms and apoptotic motility results from different possible interaction mechanisms (Fig. 3a, b):

(1) apoptotic cells are autonomously motile^{27,28} and epithelial arms associate through a run-and-chase mechanism; or (2) epithelial arms are actively involved in propelling apoptotic targets. Analysis of F-actin and myosin-II dynamics in motile apoptotic cells *in vivo* showed static intracellular localization patterns and an absence of cell protrusions or polarized cortical localizations (Extended Data Fig. 7a, b and Supplementary Videos 9, 12). Co-expression of Bax with dominant-negative versions of proteins that regulate motility, such as Rho GTPases Rac1 and RhoA²⁹, or the downstream target Rock2a did not affect apoptotic cell speed, epithelial arm formation or phagocytic uptake (Extended Data Fig. 7c, d), suggesting that apoptotic cells do not have autonomous motility. Embryo injection with annexin-V blocked apoptotic motility and arm formation (Extended Data Fig. 7e, f), indicating a role of PS recognition in target movement. Apoptotic motility was always associated with epithelial arms ($n = 59$ out of 59 motile cells, 6 embryos) (Extended Data Fig. 9g, h and Supplementary Video 12), suggesting that it is specifically driven by these protrusions. Three-dimensional co-cultures of apoptotic and live progenitor cells showed no apoptotic cell motility or polarized F-actin accumulation in the absence of epithelial cells (Extended Data Fig. 7i, j). Ubiquitous expression of dnRac1 in the whole embryo blocked apoptotic cell motility along with the formation of epithelial arms and phagocytic uptake (Fig. 3c–e, Extended Data Fig. 7k, l and Supplementary Video 13).

To directly test whether epithelial arms can exert mechanical forces to move apoptotic cells *in vivo*, we transferred lipid-based surrogate apoptotic targets into the embryo. PS⁺ targets moved similarly to apoptotic cells with phases of high speed (Fig. 3f–h and Supplementary Video 13) and contact-dependent formation of epithelial actin-rich arms (Fig. 3f), which was absent in PS⁻ targets (Fig. 3g, h), indicating that epithelial arms propel apoptotic particles *in vivo*. Inhibition of actin polymerization factors, such as the Arp2/3 complex, with CK-666 or Formin proteins with SMIFH2 blocked phagocytosis of apoptotic cells (Fig. 3i, k, l). Arp2/3

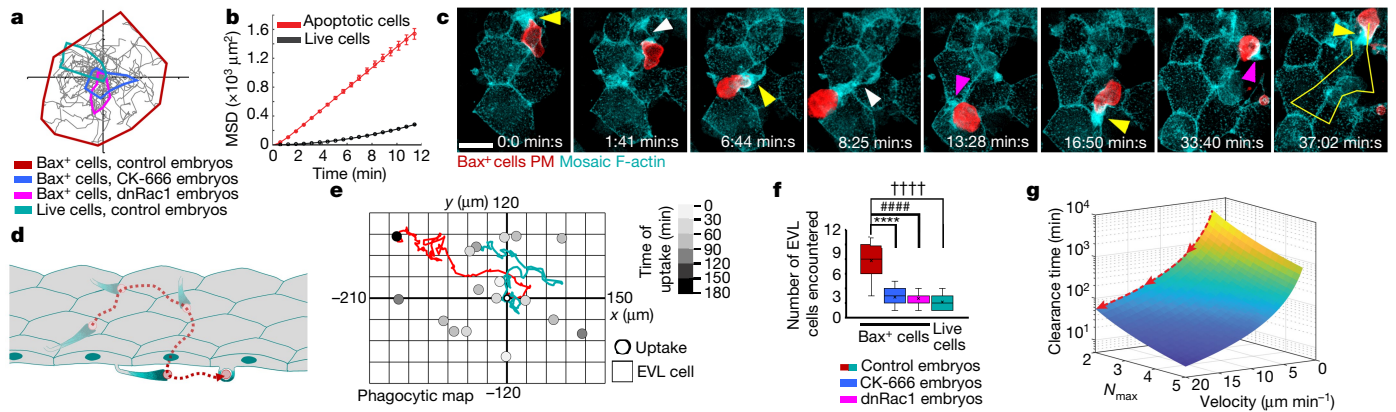


Fig. 4 | Epithelial cells cooperate through active target spreading to improve the efficiency of tissue clearance. **a**, Representative spreading areas of apoptotic cells in control, CK-666-treated and dnRac1 embryos, and of live cells in control embryos. **b**, Mean square displacement (MSD) analysis of apoptotic and live cells ($n = 29$ and 23 cells, respectively, from 4 embryos), with persistent random walk behaviour versus slower directional flow for apoptotic and live cells. Data are mean \pm s.e.m. **c**, Pushing from different epithelial arms creates an apoptotic Bax⁺ cell movement path (yellow line). Arrowheads indicate new arm formations (magenta), arm pushing phases (yellow) and retraction-associated thinning (white). The embryo is double mosaic for Bax/Lyn-tdTomato (plasma membrane) and Lifeact-GFP expression. **d**, Schematic showing apoptotic target movement by consecutive arm pushing before

phagocytic uptake. **e**, Spatiotemporal uptake map of single phagocytic events (grey circles) and two representative apoptotic cell paths (red, cyan). All events were centred to the origin ($n = 17$ cells from 4 embryos). Squares of the grid represent single epithelial cells. **f**, Number of EVL cells encountered by individual apoptotic cells before uptake in control, CK-666-treated and dnRac1 embryos, and live cells in control embryos in an equivalent time period ($n = 17$ cells from 4 embryos per condition). Box plot shows the maximum and minimum (whiskers), medians (lines), 25th and 75th percentiles (boxes) and means (crosses). Unpaired one-way ANOVA and Tukey's multiple comparison test, **** $P = 9.75 \times 10^{-12}$, ### $P = 9.63 \times 10^{-12}$, **** $P = 9.57 \times 10^{-12}$. **g**, Plot of clearance time versus N_{\max} and target pushing velocity for a total number of targets $N_{\text{target}} = 15$. Scale bar, $20 \mu\text{m}$ (c).

but not Formin interference also inhibited arm formation and apoptotic motility (Fig. 3j,m, n and Supplementary Video 13), suggesting that epithelial arm protrusions primarily depend on Arp2/3 network branching activity³⁰. Our data show that epithelial cells establish two types of Rac1-dependent actin-based protrusions (Fig. 3a): phagocytic cups, which mediate target uptake, and epithelial arms, which promote apoptotic target movement by mechanical pushing.

Clearance by mechanical cooperation

At the global tissue scale, epithelial arms mechanically disperse apoptotic targets along the epithelial surface before uptake, compared with conditions that inhibited arm formation (Fig. 4a). Mean square displacement analysis of apoptotic cell paths showed that target movement followed a persistent random walk (Fig. 4b), with periods of fast and directional motility during epithelial arm contacts and random directional changes between consecutive arm interactions (Fig. 4c and Supplementary Video 14). The path of an apoptotic cell therefore emerges by the collective mechanical action of multiple epithelial cells (Fig. 4d). Apoptotic targets travelled long distances before uptake ($d = 437 \pm 49 \mu\text{m}$ (mean \pm s.e.m.)), facilitating uptake at distant locations and increasing encounters with epithelial cells (Fig. 4e, f), recruiting more phagocytes for clearance. Local transplantation of apoptotic cells underneath the EVL directly confirmed cluster dispersal (Extended Data Fig. 8a and Supplementary Video 14) with an effective spreading area of $2 \times 10^4 \mu\text{m}^2$ (about 22 epithelial cells) in 1 h. Whereas professional phagocytes are motile to reach their targets³¹, this process is inverted during epithelial clearance with targets moving around multiple non-motile phagocytic cells. These data support the cooperative mechanical interaction of multiple epithelial cells during tissue clearance, a process we refer to as mechanical load-sharing.

To assess how mechanical dispersal influences apoptotic clearance dynamics, we performed Monte Carlo simulations of apoptotic target spreading and uptake, parameterized by the pushing probability p_p , the speed v and pushing period τ . Target uptake by epithelial cells, each of lateral extent L , occurs with probability p_{up} and is limited by the maximum uptake capacity of individual epithelial cells N_{\max} (Extended

Data Fig. 8b), as documented in professional phagocytes^{32,33}. Assuming a localized initial accumulation of apoptotic targets N_{target} , simulation kymographs showed a characteristic target dispersal with an effective diffusion constant D_{eff} (Extended Data Fig. 8c and Supplementary Note 1). Spreading enabled apoptotic target uptake within an expanding area of the epithelium in which cells have not reached their uptake limit N_{\max} yet. Faster target dispersal decreased total tissue clearance time t_{clear} (Fig. 4g and Extended Data Fig. 8c, d), with t_{clear} varying as $\propto 1/v^2$ as obtained from an analytical derivation of the total clearance time (Supplementary Note 1). This mechanism is highly effective even under conditions when an increased number of localized targets (N_{target}) has to be cleared by circumventing local phagocytic saturation, with t_{clear} varying as $\propto (N_{\text{target}}/N_{\max})^2$ (Extended Data Fig. 8e–g). Our modelling suggests that target spreading through mechanical-load sharing enables the cooperative uptake of apoptotic cells, which considerably extends the limited spatial exploration and uptake range of individual epithelial cells to optimize tissue clearance.

To analyse epithelial uptake efficiency in vivo, we transplanted a large amount of apoptotic Jurkat cells (282 ± 22) (Extended Data Fig. 9a, b). Target uptake by single epithelial cells increased until a characteristic plateau was reached after about 140 min (2.8 ± 0.3 targets) (Extended Data Fig. 9b–d), even though apoptotic targets were available in contact with the basal epithelial surface (Extended Data Fig. 9c, e). This indicates that epithelial cells have an intrinsic limit in their uptake capacity N_{\max} . Neighbouring epithelial cells located outside of saturated epithelial areas further engaged in the clearance process over time (Extended Data Fig. 9f). Considering the maximum uptake volume V_{\max} per epithelial cell ($V_{\max} = 1,200 \pm 60 \mu\text{m}^3$, Extended Data Fig. 9g, h; representing about 18% of an average epithelial cell volume $V_{\text{EVL}} = 6,648 \pm 297 \mu\text{m}^3$) and an average apoptotic cell volume $V_{\text{target}} = 2,400 \pm 200 \mu\text{m}^3$, a single epithelial cell is limited to clear about 0.5 apoptotic cells. This makes mechanical target dispersal relevant for both low and high numbers of apoptotic cells and ensures rapid clearance by engaging more phagocytes in the uptake process. Similarly, professional phagocytes often operate in groups, with the number of recruited phagocytes being proportional to the mass that needs to be cleared for improving uptake efficiency^{31,34,35}.

We reveal a previously undescribed evolutionarily conserved function for epithelia as efficient scavengers of apoptotic cells in the earliest stages of vertebrate embryogenesis. This clearance system is relevant for error correction and developmental robustness in the presence of both sporadic cell death and failures involving larger regions that compromise embryo survival, emulating roles of the immune system in adult tissues. Epithelial phagocytosis regulates tissue homeostasis and inflammation in specific organs of the adult organisms^{3,36,37} and in immune-privileged tissues such as the retina and the testis³⁸. Here we show that during early vertebrate development, epithelial cells specialize to perform phagocytic immune functions in the complete absence of immune cells. At later developmental stages, professional phagocytes differentiate and can share their phagocytic tasks with mesenchymal or epithelial cells^{39–42}. Epithelial protection mechanisms in other early developmental contexts should be further explored, as phagocytic functions were also identified in invertebrate embryos^{43–46}.

Whereas the chemical cooperation between cells has been well-documented, mechanical cooperation as a physiological tissue function remains poorly understood. Overall, our results indicate that active mechanical target distribution promotes phagocytic cooperation among epithelial cells. This can ensure the rapid and efficient clearance of apoptotic targets through a division of labour by increasing the number of phagocytes participating in uptake. Mechanical cell cooperation as a previously undescribed mechanism to improve phagocytic clearance can have broad relevance in pathological and physiological conditions in which phagocytic uptake plays a central part, such as in homeostatic cell turnover^{4,47} and tissue inflammation⁴⁸.

Online content

Any methods, additional references, Nature Research reporting summaries, source data, extended data, supplementary information, acknowledgements, peer review information; details of author contributions and competing interests; and statements of data and code availability are available at <https://doi.org/10.1038/s41586-021-03200-3>.

1. Schneider, I. & Ellenberg, J. Mysteries in embryonic development: how can errors arise so frequently at the beginning of mammalian life? *PLoS Biol.* **17**, e3000173 (2019).
2. Bolton, H. et al. Mouse model of chromosome mosaicism reveals lineage-specific depletion of aneuploid cells and normal developmental potential. *Nat. Commun.* **7**, 11165 (2016).
3. Juncadella, I. J. et al. Apoptotic cell clearance by bronchial epithelial cells critically influences airway inflammation. *Nature* **493**, 547–551 (2013).
4. Arandjelovic, S. & Ravichandran, K. S. Phagocytosis of apoptotic cells in homeostasis. *Nat. Immunol.* **16**, 907–917 (2015).
5. Doran, A. C., Yurdagul, A. Jr & Tabas, I. Efferocytosis in health and disease. *Nat. Rev. Immunol.* **20**, 254–267 (2020).
6. Akhtar, N., Li, W., Mironov, A. & Streuli, C. H. Rac1 controls both the secretory function of the mammary gland and its remodeling for successive gestations. *Dev. Cell* **38**, 522–535 (2016).
7. Artus, J., Kang, M., Cohen-Tannoudji, M. & Hadjantonakis, A. K. PDGF signaling is required for primitive endoderm cell survival in the inner cell mass of the mouse blastocyst. *Stem Cells* **31**, 1932–1941 (2013).
8. Akieda, Y. et al. Cell competition corrects noisy Wnt morphogen gradients to achieve robust patterning in the zebrafish embryo. *Nat. Commun.* **10**, 4710 (2019).
9. Claveria, C., Giovinazzo, G., Sierra, R. & Torres, M. Myc-driven endogenous cell competition in the early mammalian embryo. *Nature* **500**, 39–44 (2013).
10. Zhong, J. X., Zhou, L., Li, Z., Wang, Y. & Gui, J. F. Zebrafish Noxa promotes mitosis in early embryonic development and regulates apoptosis in subsequent embryogenesis. *Cell Death Differ.* **21**, 1013–1024 (2014).
11. Vanneste, E. et al. Chromosome instability is common in human cleavage-stage embryos. *Nat. Med.* **15**, 577–583 (2009).
12. Greco, E., Minasi, M. G. & Fiorentino, F. Healthy babies after intrauterine transfer of mosaic aneuploid blastocysts. *N. Engl. J. Med.* **373**, 2089–2090 (2015).
13. Elliott, M. R. & Ravichandran, K. S. The dynamics of apoptotic cell clearance. *Dev. Cell* **38**, 147–160 (2016).
14. Oltval, Z. N., Milliman, C. L. & Korsmeyer, S. J. Bcl-2 heterodimerizes in vivo with a conserved homolog, Bax, that accelerates programmed cell death. *Cell* **74**, 609–619 (1993).
15. Furniss, K. L. et al. Direct monitoring of the strand passage reaction of DNA topoisomerase II triggers checkpoint activation. *PLoS Genet.* **9**, e1003832 (2013).

16. Palchaudhuri, R. et al. A small molecule that induces intrinsic pathway apoptosis with unparalleled speed. *Cell Rep.* **13**, 2027–2036 (2015).
17. Vorsele, D. et al. Microparticle traction force microscopy reveals subcellular force exertion patterns in immune cell–target interactions. *Nat. Commun.* **11**, 20 (2020).
18. Patel, P. C. & Harrison, R. E. Membrane ruffles capture C3bi-opsinized particles in activated macrophages. *Mol. Biol. Cell* **19**, 4628–4639 (2008).
19. Schlam, D. et al. Phosphoinositide 3-kinase enables phagocytosis of large particles by terminating actin assembly through Rac/Cdc42 GTPase-activating proteins. *Nat. Commun.* **6**, 8623 (2015).
20. Jaumouillès, V., Cartagena-Rivera, A. X. & Waterman, C. M. Coupling of β_2 integrins to actin by a mechanosensitive molecular clutch drives complement receptor-mediated phagocytosis. *Nat. Cell Biol.* **21**, 1357–1369 (2019).
21. Fadok, V. A. et al. Exposure of phosphatidylserine on the surface of apoptotic lymphocytes triggers specific recognition and removal by macrophages. *J. Immunol.* **148**, 2207–2216 (1992).
22. Vieira, O. V. et al. Modulation of Rab5 and Rab7 recruitment to phagosomes by phosphatidylinositol 3-kinase. *Mol. Cell Biol.* **23**, 2501–2514 (2003).
23. Park, H. & Cox, D. Cdc42 regulates Fc gamma receptor-mediated phagocytosis through the activation and phosphorylation of Wiskott–Aldrich syndrome protein (WASP) and neural-WASP. *Mol. Biol. Cell* **20**, 4500–4508 (2009).
24. Gold, E. S. et al. Dynamin 2 is required for phagocytosis in macrophages. *J. Exp. Med.* **190**, 1849–1856 (1999).
25. Deng, Q., Ramsköld, D., Reinius, B. & Sandberg, R. Single-cell RNA-seq reveals dynamic, random monoallelic gene expression in mammalian cells. *Science* **343**, 193–196 (2014).
26. Petropoulos, S. et al. Single-cell RNA-seq reveals lineage and X chromosome dynamics in human preimplantation embryos. *Cell* **165**, 1012–1026 (2016).
27. van Ham, T. J., Kokel, D. & Peterson, R. T. Apoptotic cells are cleared by directional migration and *elmo1*-dependent macrophage engulfment. *Curr. Biol.* **22**, 830–836 (2012).
28. Yamaguchi, Y. et al. Live imaging of apoptosis in a novel transgenic mouse highlights its role in neural tube closure. *J. Cell Biol.* **195**, 1047–1060 (2011).
29. Heasman, S. J. & Ridley, A. J. Mammalian Rho GTPases: new insights into their functions from in vivo studies. *Nat. Rev. Mol. Cell Biol.* **9**, 690–701 (2008).
30. Welch, M. D., Iwamatsu, A. & Mitchison, T. J. Actin polymerization is induced by Arp2/3 protein complex at the surface of *Listeria monocytogenes*. *Nature* **385**, 265–269 (1997).
31. Lämmermann, T. et al. Neutrophil swarms require LTB4 and integrins at sites of cell death in vivo. *Nature* **498**, 371–375 (2013).
32. Zent, C. S. & Elliott, M. R. Maxed out macs: physiologic cell clearance as a function of macrophage phagocytic capacity. *FEBS J.* **284**, 1021–1039 (2017).
33. Armitage, E. L., Roddie, H. G. & Evans, I. R. Overexposure to apoptosis via disrupted glial specification perturbs *Drosophila* macrophage function and reveals roles of the CNS during injury. *Cell Death Dis.* **11**, 627 (2020).
34. Evans, I. R., Ghai, P. A., Urbančić, V., Tan, K. L. & Wood, W. SCAR/WAVE-mediated processing of engulfed apoptotic corpses is essential for effective macrophage migration in *Drosophila*. *Cell Death Differ.* **20**, 709–720 (2013).
35. Voelz, K., Gratacap, R. L. & Wheeler, R. T. A zebrafish larval model reveals early tissue-specific innate immune responses to *Mucor circinelloides*. *Dis. Model. Mech.* **8**, 1375–1388 (2015).
36. Lee, C. S. et al. Boosting apoptotic cell clearance by colonic epithelial cells attenuates inflammation in vivo. *Immunity* **44**, 807–820 (2016).
37. Serizier, S. B. & McCall, K. Scrambled eggs: apoptotic cell clearance by non-professional phagocytes in the *Drosophila* ovary. *Front. Immunol.* **8**, 1642 (2017).
38. Penberthy, K. K., Lysiak, J. J. & Ravichandran, K. S. Rethinking phagocytes: clues from the retina and testes. *Trends Cell Biol.* **28**, 317–327 (2018).
39. Zhu, Y. et al. Migratory neural crest cells phagocytose dead cells in the developing nervous system. *Cell* **179**, 74–89 (2019).
40. Wood, W. et al. Mesenchymal cells engulf and clear apoptotic footplate cells in macrophageless PU.1 null mouse embryos. *Development* **127**, 5245–5252 (2000).
41. Ellis, S. J. et al. Distinct modes of cell competition shape mammalian tissue morphogenesis. *Nature* **569**, 497–502 (2019).
42. Rasmussen, J. P., Sack, G. S., Martin, S. M. & Sagasti, A. Vertebrate epidermal cells are broad-specificity phagocytes that clear sensory axon debris. *J. Neurosci.* **35**, 559–570 (2015).
43. Fazeli, G., Stetter, M., Lisack, J. N. & Wehman, A. M. C. *elegans* blastomeres clear the corpse of the second polar body by LC3-associated phagocytosis. *Cell Rep.* **23**, 2070–2082 (2018).
44. Gumienny, T. L., Lambie, E., Hartweg, E., Horvitz, H. R. & Hengartner, M. O. Genetic control of programmed cell death in the *Caenorhabditis elegans* hermaphrodite germline. *Development* **126**, 1011–1022 (1999).
45. Nakanishi, N., Sogabe, S. & Degnan, B. M. Evolutionary origin of gastrulation: insights from sponge development. *BMC Biol.* **12**, 26 (2014).
46. Silva, J. R. The onset of phagocytosis and identity in the embryo of *Lytechinus variegatus*. *Dev. Comp. Immunol.* **24**, 733–739 (2000).
47. Lim, J. J., Grinstein, S. & Roth, Z. Diversity and versatility of phagocytosis: roles in innate immunity, tissue remodeling, and homeostasis. *Front. Cell. Infect. Microbiol.* **7**, 191 (2017).
48. Arienti, S., Barth, N. D., Dorward, D. A., Rossi, A. G. & Dransfield, I. Regulation of apoptotic cell clearance during resolution of inflammation. *Front. Pharmacol.* **10**, 891 (2019).

Publisher's note Springer Nature remains neutral with regard to jurisdictional claims in published maps and institutional affiliations.

© The Author(s), under exclusive licence to Springer Nature Limited 2021

Reporting summary

Further information on research design is available in the Nature Research Reporting Summary linked to this paper.

Data availability

RNA-sequencing data and analyses are available in Supplementary Table 1, and raw data have been deposited in the Gene Expression Omnibus (GEO) under accession number GSE143734. Raw microscopy data are available from the corresponding authors upon request due to their large file sizes. Source data are provided with this paper.

Code availability

RNA-sequencing data were analysed using published processing pipelines as outlined in detail in the Supplementary Methods. Image analysis routines are described in the Supplementary Methods. Image analysis and simulation codes are available on GitHub (<https://github.com/stefanwieser/Clearance.git>).

49. Shinoda, H., Shannon, M. & Nagai, T. Fluorescent proteins for investigating biological events in acidic environments. *Int. J. Mol. Sci.* **19**, 1548 (2018).
50. Delamarre, L., Pack, M., Chang, H., Mellman, I. & Trombetta, E. S. Differential lysosomal proteolysis in antigen-presenting cells determines antigen fate. *Science* **307**, 1630–1634 (2005).

Acknowledgements We thank T. Graf, B. Lehner and V. Malhotra for discussions and reading of the manuscript. Q.T.-R. acknowledges a grant funded by 'The Ministerio de Ciencia, Innovación y Universidades and Fondo Social Europeo (FSE)' (PRE2018-084393). M.I. acknowledges funding from the European Research Council (ERC) under the European Union's Horizon 2020 research and innovation program (ERC-StG-LS2-63759) and the Spanish Ministry of Economy and Competitiveness (BFU2014-55076-P). S.W. acknowledges support from the Government of Spain (MINECO's Plan Nacional (PGC2018-098532-A-I00), Severo Ochoa (CEX2019-000910-S)), Fundació Cellex, Fundació Mir-Puig and Generalitat de Catalunya (CERCA, AGAUR). V.R. acknowledges support from the Spanish Ministry of Science and Innovation to the EMBL partnership, the Centro de Excelencia Severo Ochoa, MINECO's Plan Nacional (BFU2017-86296-P), Generalitat de Catalunya (CERCA) and support from the CRG Core Facilities for Genomics, Biomolecular Screening and Protein Technologies, Flow Cytometry and Advanced Light Microscopy.

Author contributions E.H. designed research, performed experiments and analysed data. H.-M.H. contributed to in vivo experiments and data analysis. Q.T.-R. contributed to in vitro experiments. S.J.-D. supported cloning and mRNA injections. C.W. performed sequencing analysis. M.M.-C. contributed to mouse blastocyst experiments. M.I. supervised C.W. and M.M.-C. and performed sequencing analysis. A.C.-J. performed theoretical modelling. S.W. analysed data and performed Monte Carlo simulations. V.R. designed research, performed data analysis and supervised the project. E.H. and V.R. wrote the manuscript with contributions from all of the authors.

Competing interests The authors declare no competing interests.

Additional information

Supplementary information The online version contains supplementary material available at <https://doi.org/10.1038/s41586-021-03200-3>.

Correspondence and requests for materials should be addressed to E.H., S.W. or V.R.

Peer review information Nature thanks Jean-Léon Maître and the other, anonymous, reviewer(s) for their contribution to the peer review of this work.

Reprints and permissions information is available at <http://www.nature.com/reprints>.